ACSNANO

www.acsnano.org

ARTICLE

Chiral, Magnetic, and Photosensitive Liquid Crystalline Nanocomposites Based on Multifunctional Nanoparticles and Achiral Liquid Crystals

Anna Poryvai, Michal Šmahel, Marie Švecová, Ahlam Nemati, Sasan Shadpour, Pavel Ulbrich, Timothy Ogolla, Jiao Liu, Vladimíra Novotná, Miroslav Veverka, Jana Vejpravová, Torsten Hegmann, and Michal Kohout*

Cite This: *ACS Nano* 2022, 16, 11833–11841

Read Online

ACCESS | Metrics & More | Article Recommendations | Supporting Information

ABSTRACT: **Nanoparticles serving as a multifunctional and multiaddressable dopant to modify the properties of liquid crystalline matrices are developed by combining cobalt ferrite nanocrystals with organic ligands featuring a robust photosensitive unit and a source of chirality from the natural pool. These nanoparticles provide a stable nanocomposite when dispersed in achiral liquid crystals, giving rise to chiral supramolecular structures that can respond to UV-light illumination, and, at the same time, the formed nanocomposite possesses strong magnetic response. We report on a nanocomposite that shows three additional functionalities (chirality and responsiveness to UV light and magnetic field) upon the introduction of a single dopant into achiral liquid crystals.**

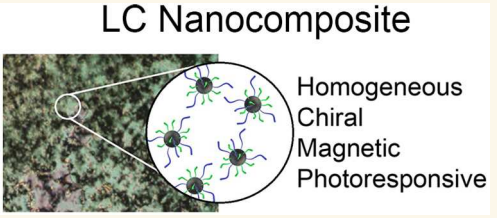

KEYWORDS: *multifunctional nanoparticles, nanocomposites, magnetic nanoparticles, liquid crystals, smart organic materials*

Liquid crystalline (LC) materials are widely used due to their ability to form defined supramolecular structures (mesophases). Depending on the molecular structure of the constituent mesogens, the supramolecular organization of mesophases can be tuned by various external stimuli, such as temperature, mechanical stress, light, and electric and magnetic fields. To induce, for example, spatially twisted molecular arrangements (chirality) or improve the responsiveness of mesophases, *e.g.*, toward light or magnetic fields, specifically designed dopants can be added to LC hosts.

Chiral dopants, for example, inducing chirality in achiral LC hosts, are of particular interest since certain chiral mesophases readily respond to an applied electric field and can be utilized for the fabrication of LC displays and other devices. A great number of chiral scaffolds, such as lactic acid,[1] 1,2-dioles,[2] TADDOL,[3] atropisomeric biphenyls,[4] helicenes,[5] or Ru complexes,[6] have been implemented into the structures of chiral additives. Currently, the utilization of chiral compounds from the natural pool is in the spotlight due to their high optical purity, availability on a large scale, and low cost.

Photoresponsive dopants (PDs) are added to LC hosts to induce photoresponsivity of mesophases, since light-driven phase transition is of high interest from both scientific and technological points of view.[7] PDs of high structural diversity and the type of photoinduced structural change are known to date.[8] Such PDs include those with a carbon−carbon double bond (*E*/*Z*-isomerization and [2+2] cycloaddition),[9] spiropyran-based systems,[10,11] dithienyl ethenes (open−closed ring isomerization),[12] and materials containing a diazenyl group (*E*/*Z*-isomerization), to name a few. Currently, the diazenyl group is frequently used as a source of photoresponsivity, mainly due to its chemical stability and lower energies of the *E*/*Z*-isomerization combined with its easy introduction into a structure through the azo-coupling reaction.[8,13,14]

Response toward magnetic fields is usually induced by addition of organometallic complexes[15] or magnetic nanoobjects.[16−18] Miscibility of such dopants with LC hosts is a limiting parameter for their application, which is especially crucial for magnetic nanoparticles (MNPs). It has been shown that for stabilization of MNPs in LC hosts their surface should

Received: November 29, 2021
Accepted: July 18, 2022
Published: July 22, 2022

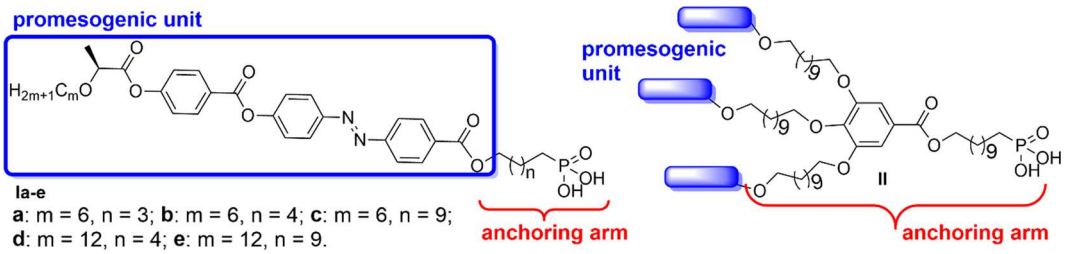

Figure 1. Structure of ligands Ia−e and II.

be properly modified by ligands that mimic the structure of the LC host.[19] Ligands bearing one or more mesogenic (promesogenic) units with various anchoring groups are most frequently utilized.[20] Although many nanocomposite materials have been studied so far, only few studies concern ligands that serve not only as stabilizers of the NPs but also as the chiral dopants or PDs.[21−28]

Gold nanoparticles (NPs) and nanorods have been the most frequently studied carriers for various chiral dopants and used as functionalized additives for thermotropic LCs. BINOL,[21,23] cholesterol,[22,26] or naproxene units were successfully used as a source of chirality in the developed ligands attached to the surface of gold nanoobjects. Gold and silver NPs covered with azobenzene-based ligands have been reported to form photoresponsive mesophases as bulk materials.[28] It has been documented that the process of *Z*- to *E*-relaxation of the ligands attached to the NPs is significantly faster than that of the free ligands in a solution. In addition, a nanomaterial based on gold NPs covered with ligands containing a diazenyl linker, which restore its ground state mesomorphic properties even after 10 cycles of photoinduced switching, has been reported.[25] Photosensitive ligand mixtures attached to the surface of gold NPs gave rise to nanomaterials exhibiting photoresponsivity at room temperature[24] or UV-light-responsive surface plasmon resonance in a condensed state.[27] However, it should be stressed that these case studies were performed on modified photosensitive NPs as bulk materials. In general, there is only a limited number of studies using chiral photosensitive ligands bonded to NPs utilized as dopants in liquid crystals.[29]

For the current study, we decided to develop multifunctional additives, which induce all above-mentioned responses *via* enhanced functionality of the ligands. For this purpose, we have prepared cobalt ferrite nanoparticles (as a source of magnetoresponse) covered with chiral photosensitive ligands. The structures of the ligands consisted of an anchoring arm bearing one or three promesogenic units. The anchoring arms contained a phosphonic anchoring group, as it exhibits the strongest binding with the surface of cobalt ferrites.[19,30−35] The structure of the promesogenic units was based on chiral photoresponsive LC materials developed earlier in our group,[36] where lactic acid was utilized as the source of chirality. The photoresponsivity of the designed ligands was assured by a diazenyl group implemented in the central core.

RESULTS AND DISCUSSION

For this purpose, two types of ligands, linear **Ia−e** and trimeric **II**, were prepared (Figure 1). In order to study structure−property relationships, ligands of series **I** featured alkyl chains of various lengths bearing an anchoring phosphonic group. Lactic acid based chiral units were synthesized according to a previously reported procedure, which was developed in our laboratory in order to avoid racemization of the chiral building blocks.[37] Synthesis of an azobenzene-based central core and anchoring arms was described earlier.[38,39] Synthesis of the intermediates and target structures and their spectroscopic characterization are given in the Supporting Information.

Photoresponse of the prepared ligands **Ia−c** was studied using ^{1}H NMR spectroscopy. It was determined that the length of the alkyl chain bearing the anchoring phosphonic group had a negligible effect on the value of relaxation rate constants (k_r = 5×10^{-5} and 7×10^{-5} s^{-1} for C5 and C11 spacers; see Section 4, Supporting Information). Moreover, comparing the results with LCs of parental structure,[36] the presence of the phosphonic group in the structure, which induced an amphiphilic character of the ligands, had only a negligible effect on the relaxation process. A relaxation rate constant of the ligand **II** in the solution was studied using UV−vis spectroscopy at room temperature (see Section 4, Supporting Information). The value of $k_r = 3 \times 10^{-5}$ s^{-1} indicates that the *Z*-form of ligand **II** is slightly less stable than that of ligands **I**.

Ligands Ic and II were used to modify the surface of cobalt ferrite NPs covered with oleic acid using a ligand exchange strategy. Ligand **Ic** was selected as a model material to optimize the strategy (see Section 5, Supporting Information). First, NPs were covered with ligand **Ic** only using a described method.[40] The modification was successful (based on Fourier transform infrared spectroscopy (FT-IR) and elemental analysis (EA) data); however, the resulting nanomaterial **NPs-1** aggregated. This could be caused by an adverse orientation of the ligands in the ligand shell, namely, by interactions of the aromatic units of ligands with the surface of the NPs (Figure S6, Supporting Information).[41]

Hence, the ligand exchange strategy was further optimized using a cosurfactant in a mixture with the promesogenic ligand. As a cosurfactant, hexylphosphonic acid (HPA) was used since it possesses a shorter aliphatic chain than the anchoring arm of **Ic**, which should prevent its interference with the LC host. Modification of the MNP surface was performed in a shaker without heating (**NPs-2**) or in a pressure tube and heating to 85 °C (**NPs-3**). **NPs-2** were still aggregating while **NPs-3** were practically homogeneous as derived from transmission electron microscopy (TEM) image analysis (Figure S7, Supporting Information). Results from elemental analysis documented that higher ligand surface coverage was achieved in the case of **NPs-3** than for **NPs-2**. The ligand/cosurfactant ratio on the surface of the NPs was calculated from the results of elemental analysis assuming that all nitrogen atoms in the sample belonged to ligand **Ic**. It should be stressed that the ligand/cosurfactant ratio on the surface of NPs (found to be 9/1 or 10/1) differed from their ratio in the reaction mixture (4/1). This is in contradiction to known literature,[42] where the ratio is assumed identical in the reaction mixture and on the NPs' surface.

In order to further improve the homogeneity of MNPs, the trimeric ligand **II** was introduced using a similar setup to that

https://doi.org/10.1021/acsnano.1c10594
ACS Nano 2022, 16, 11833−11841

for **NPs-3** (Table S2, Supporting Information). As the anchoring arm of ligand **II** is longer than that of **Ic**, a longer cosurfactant (dodecylphosphonic acid, DPA) was used for the preparation of **NPs-4**. FT-IR spectroscopy (Figure S8, Supporting Information) supports the presence of ligands **II** on the surface of **NPs-4**. Results of elemental analysis have shown that the ligand/cosurfactant ratio was 1/38 or 1/13 when calculating the ratio to one diazenyl group. Thermogravimetric analysis (TGA; Figure S9, Supporting Information) revealed high thermal stability of **NPs-4** with only a negligible weight loss (Δm = 1.2%) until 320 °C. TEM image analysis showed that **NPs-4** were perfectly homogeneous (Figure 2).

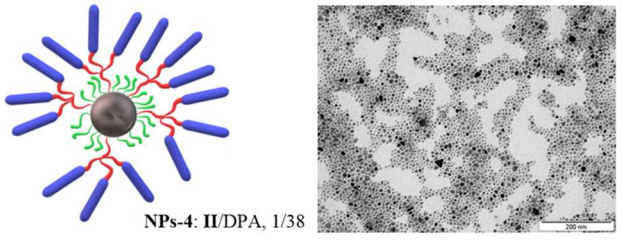

Figure 2. Schematic representation of the structure of nanomaterial NPs-4 (left) and its TEM image (right). In the schematic picture (left), the promesogenic units are depicted in blue, anchoring arms in red, DPA in green color, and the MNP as a black sphere.

We have used homogeneous **NPs-3** and **NPs-4** for the preparation of the LC nanocomposites (NCs). The detailed procedure for the preparation of NCs is described in Section 6, Supporting Information. It should be noted that **NPs-3** and **NPs-4** were immiscible with commercial room-temperature nematogens such as **5CB** or **E7**, likely due to their polar nature. Therefore, we screened several hosts, **LC-A**–**LC-D**, with a different number of aromatic rings and lateral substituents (Figure 3), which can be considered as structural analogues of ligands used for MNP modification.

NPs-3 covered with the linear ligand **Ic** formed stable nanocomposite materials **NC-1**–**3** with **LC-A** and **LC-B**, however, containing small aggregates as derived from TEM image analysis. In the **LC-C** these NPs formed large aggregates (**NC-4**), and they spontaneously precipitated from **LC-D**; therefore **NC-5** was impossible to prepare. Due to this result, **LC-D** was henceforth not further pursued for NC development (Table 1).

NPs-4 (decorated with the trimeric ligand **II**) were also used as dopants in various LC hosts (Table 1): **LC-A**, **-B**, and **-C**.

Table 1. Nanocomposites NC-1–NC-10 Based on NPs-3 and NPs-4 Selected as Dopants

Code	Host	NPs	Cosurfactant	Mixtures LC + NPs@Ligands	
				NPs, *wt%*	Homogeniety
NC-1	**LC-A**	**NPs-3**	**HPA**	0.5	✓
NC-2				1.0	✓
NC-3	**LC-B**			0.3	✓
NC-4	**LC-C**			0.3	✗
NC-5	**LC-D**			0.2	—*
NC-6	**LC-A**	**NPs-4**	**DPA**	0.5	✗
NC-7	**LC-A**			1.0	✗
NC-8	**LC-B**			0.3	✓
NC-9	**LC-B**			3.0	✗
NC-10	**LC-C**			0.3	—*

*Impossible to prepare.

First, **NC-6** and **NC-7** containing 0.5 and 1.0 *wt* % **NPs-4** in **LC-A**, respectively, were prepared. These NCs were designed based on the results obtained for **NPs-3** assuming a similar behavior of **NPs-4** and **NPs-3** due to an identical promesogenic unit in the structure of their ligand shell. However, in contrast to this assumption, NPs in **NC-6** and **NC-7** aggregated, which was apparent from polarizing optical microscopy (POM) observations.

Further investigations have shown that **NC-8** based on **LC-B**, containing one lateral chlorine substituent, did not contain aggregates (Figure 4), whereas NPs in **NC-9** aggregated

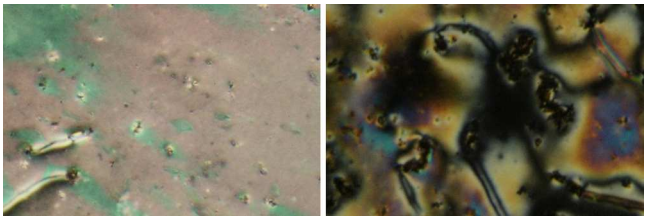

Figure 4. POM image of NC-8 (left) and NC-9 (right) in glass cells (width 12 μm).

because of the higher NP concentration. The introduction of the second lateral chlorine substituent into the structure of the host (**LC-C**) resulted in spontaneous aggregation of the NPs in **NC-10**.

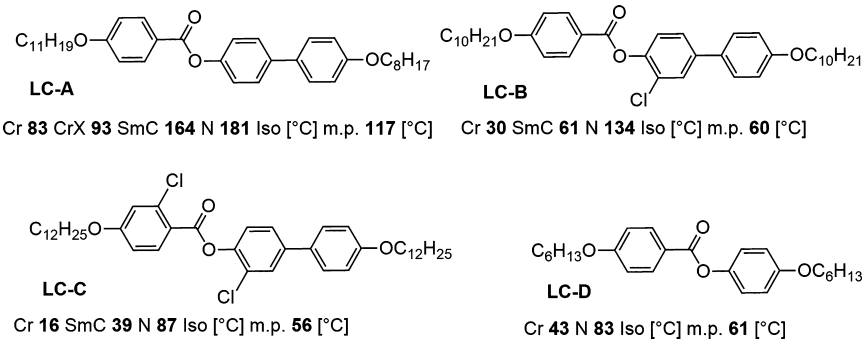

Figure 3. Structures and mesomorphic properties of liquid crystalline hosts LC-A–LC-D used for the preparation of nanocomposites.

https://doi.org/10.1021/acsnano.1c10594
ACS Nano 2022, 16, 11833–11841

Table 2. Example of UV-Light-Induced Changes of Planar Textures of the NC-8

Phase	T, °C	Before UV	Under UV	After UV
N*	127	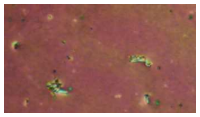	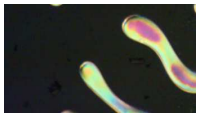	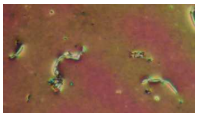
SmC*	55	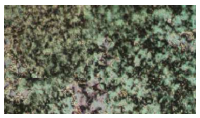	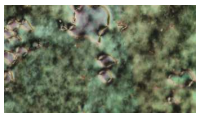	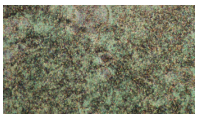

The photoresponsivity of stable nanocomposites **NC-3** and **NC-8** was studied in glass cells (width 12 μm) upon irradiation with UV light (λ = 365 nm) using POM. Melted samples were cooled to their corresponding mesophases (N* or SmC*). Both NCs have shown a similar response (changes in textures of **NC-3** are depicted in Table S4). Photos of changes in textures of **NC-8** induced by UV light (Table 2) document that the N* phase transitioned to an isotropic phase; to document the change, small areas of highly birefringent N* phase are shown in the picture. The illumination of the SmC* phase did not induce such a phase transition, but a certain degree of reorganization of the molecules within the mesophase is apparent from POM observations.

The absence of a photoresponse of the supramolecular structures at temperatures lower than 10 °C below the phase transitions temperatures may indicate overheating of the sample caused by absorption of the UV light. However, a SmC* to N* phase transition was not observed, and, therefore, it is assumed that the observed changes are induced by the transformation of the predominant *E*-isomer present in the ligands into the *Z*-isomer. The rather weak effect of UV light observed in the SmC* phase can be related to the overall low concentration of the nanomaterial. This is consistent with the extent of chiral induction observed for **NC-8** (*vide infra*).

LC-B as a neat material (Figure S11, Supporting Information) and **LC-B** doped with **NPs-4** (**NC-8**) were also analyzed by circular dichroism (CD) spectropolarimetry both in solution for neat **NPs-4** (Figure S12, Supporting Information) and in thin films of the doped bulk material (Figure 5). Currently, advanced techniques (such as Mueller matrix polarimetry) allowing for variation of the azimuthal orientation of the measured thin film sample are frequently used to determine induced chirality of a material,[43−45] preferentially to CD measurements.[46] However, thin film CD of bulk materials has also been successfully used to determine the induction of chirality, particularly in LC phases.[21−23,47−50] Since the equipment for measuring induced circular dichroism determination has been available to our team, we decided to use this technique to assess chirality induction in the studied sample. Figure 5 shows the thin film CD spectra collected for **LC-B** doped with 0.3 *wt* % **NPs-4** (**NC-8**) in thin films (~20 μm gap) between two precleaned quartz substrates at 40 °C in the host SmC and at 75 °C in the host N-LC phase. To eliminate (or cancel out) contributions from linear dichroism and birefringence of the induced N* and SmC* phases, the interrogated sample areas were investigated at all sample rotation angles in 45° intervals. The obtained thin films' CD spectra were then summed up to provide genuine CD signals of the sample area. The circular area interrogated by the light

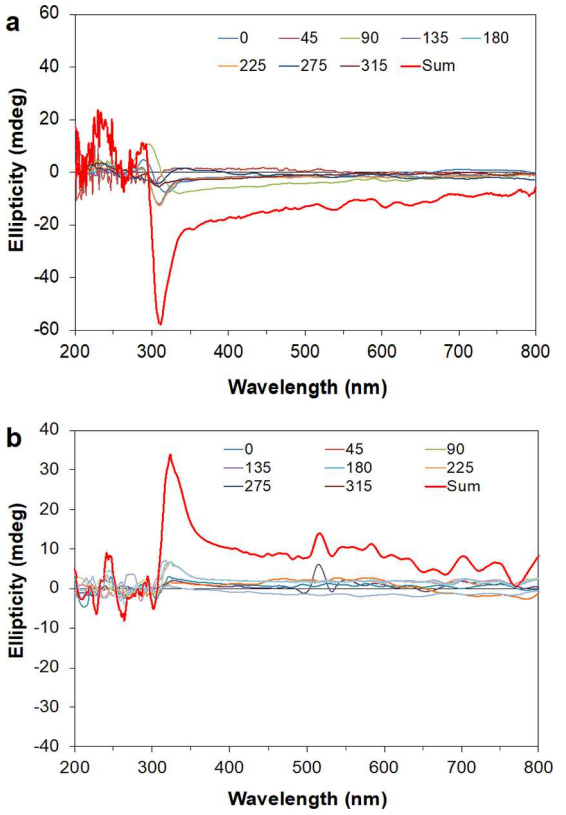

Figure 5. Thin film CD spectra (film thickness: 20 μm) of LC-B doped with 0.3 wt % NPs-4 at (a) 40 °C (in a SmC* mesophase) and (b) at 75 °C (in a N* mesophase). For corresponding UV−vis spectra please see Figures S13−S15, Supporting Information.

beam is approximately 0.4 cm in diameter (given by the instrumental slit size and shape), which was significantly larger than the typical size of domains in the induced N* and SmC* phases observed by POM. Therefore, the bulk of the sample is measured and not just individual domains. Each sum-CD spectrum shows clearly discernible negative or positive sum-CD signals with a maximum ellipticity centered around 320 nm, thereby supporting the assumption that **NPs-4** induce a bulk SmC* and N* phase, respectively. The thin film CD spectra also supported the microscopy observations indicating the aggregation of **NPs-4** in **LC-B** above 0.3 wt %, showing random and very noisy CD signals that could not be interpreted.

Magnetic properties of the **NC-3** and **NC-8** samples were also investigated and compared to the data obtained for the original NPs. Temperature dependencies of the magnetization

https://doi.org/10.1021/acsnano.1c10594
ACS Nano 2022, 16, 11833−11841

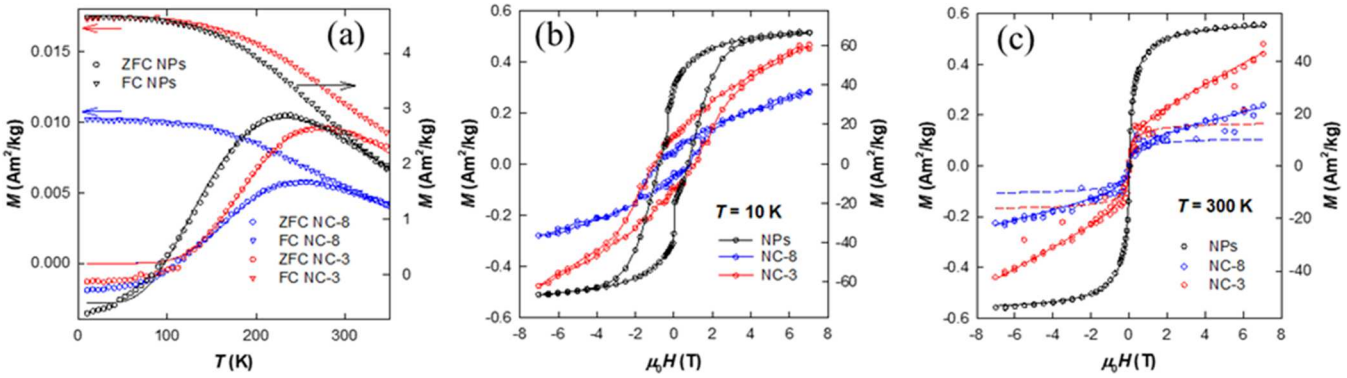

Figure 6. Magnetic properties of the NPs, NC-8, and NC-3 samples. Please note the different scale in the *y*-axis for the NPs as well as NC-8 and NC-3 samples, as shown by the black, red, and blue arrows in panel (a). The temperature dependencies of zero-field-cooled (ZFC) and field-cooled (FC) magnetization recorded at 10 mT are presented in panel (a). The solid lines correspond to the fit using eq S1. Magnetization isotherms measured at 10 and 300 K are shown in panels (b) and (c), respectively. The solid lines in panel (c) correspond to the best fit using the nonregularized inversion method (eq S4 and MINORIM[51]), and the dashed lines show the pure Langevin component after subtraction of the linear contribution (samples NC-8 and NC-3 only).

recorded in the zero-field-cooled (ZFC) and field-cooled (FC) modes are shown in Figure 6a.

The trend corresponds very well to the $CoFe_2O_4$ NPs prepared *via* the same method and functionalized with oleic acid or organic ligands of similar dimensions.[52] The ZFC curves follow a typical trend with a log-normal distribution of the blocking temperatures (T_B) originated from the distribution of the particle volumes and effective energy barriers.[53,54] The FC curves show a saturation at low temperatures, which is usually assigned to the interparticle interactions. This behavior is a common fingerprint of FC curves in dense systems of NPs, like powders and concentrated ferrofluids.[54,55]

Upon closer inspection, we can unravel moderate changes in the T_B. The original NPs functionalized with oleic acid reveal the lowest value of the T_B at the maximum of the ZFC curve of ~230 K, while the **NC-3** and **NC-8** samples show T_B values of ~250 and ~268 K, respectively. Complete analysis of the ZFC curve using the fit of the log-normal distribution confirmed the same trend for the mean T_B values (please see Table S5). Furthermore, the distribution width is comparable for all three samples, suggesting that the particle size distribution was not affected during the ligand exchange procedures. Thus, the observed changes can be solely attributed to the modification of the surface layer and interparticle distance in the powder; both effects induce a change of the effective magnetic anisotropy (represented by the effective anisotropy constant, K_{eff}) of the particles.[54] (For details of the analysis and complete set of results, please see Section 7, Supporting Information.)

The suggested scenario is also supported by the character of the magnetization isotherms measured in the blocked ($T < T_B$) and superparamagnetic ($T > T_B$) regime (Figure 6b and c). Hysteresis loops clearly open in the blocked state. The coercive field, H_C^{10K}, increases moderately from 0.75 T for the precursor NPs to 0.82 and 1.04 T for the **NC-8** and **NC-3** samples, respectively. The increase of the coercivity in single-domain $CoFe_2O_4$ NPs is typically associated with the strengthening of the interparticle interactions and enhancement of the K_{eff} due to the surface spin layer modification.[48] An additional signature of the later effect is the dramatic change of the loop shape. While the original particles show a common shape of the hysteresis loop with a squareness value of ~0.75, which is typical for the $CoFe_2O_4$ NPs of a comparable size,[52,55] the magnetization curves of the **NC-8** and **NC-3** samples show an additional strong paramagnetic-like contribution. The same term also dominates the magnetization isotherms of these samples in the superparamagnetic regime (Figure 6c), while the magnetization of the original particles shows a common Langevin-type shape.[56]

Besides the coercivity, another important parameter one can obtain from the analysis of the magnetization curves is the saturation magnetization, M_s. In our samples, the M_s of the precursor NPs reaches 70 Am^2/kg at 300 K, which is in very good agreement with the values reported for the $CoFe_2O_4$ NPs of similar size produced by the hydrothermal method.[52] The M_s values of the **NC-8** and **NC-3** samples (obtained from the extracted Langevin component at 300 K; please see Figure 6c and Section 7, Supporting Information, for details of the analysis) were found to be 12 and 18 Am^2/kg. The obtained results suggest that the content of the magnetic phase is about 17 and 25 wt % in the **NC-8** and **NC-3** samples, respectively. However, in fine particles with a surface coating, the absolute M_s values are strongly influenced by the uncertainty in the organic content determination; thus, they are not relevant for a deeper discussion of the coating effect on the spin structure.

Let us turn our attention to the extra paramagnetic-like contribution, which is a striking difference between the magnetization isotherms of the original particles and the composites. Such "lack of saturation" is often associated with the surface spin layer of the particles, which retains considerable spin disorder and frustration.[57−59] The reason is that surface spins are easily influenced by either bonding or nonbonding interactions with the surroundings such as the ligands, adsorbates, and other magnetic nanoparticles. Also, the intrinsic surface effect due to the dangling bonds and local symmetry breaking giving rise to the nonzero orbital contribution to the magnetic moment contribute to the increase of the K_{eff} and force the spins to decline from the bulk magnetic structure. On the other hand, it has been shown recently that the spin canting can also propagate through the whole volume of the particles, in the hard spinel ferrites with extremely good crystallinity.[60,61]

In order to decide on the dominant mechanism behind the observed changes, we carried out further analysis of the magnetization isotherms above the T_B. As an important parameter, we evaluated the mean value of the magnetic moment per particle (μ_m) using two complementary

https://doi.org/10.1021/acsnano.1c10594
ACS Nano 2022, 16, 11833−11841

approaches (please see Section 7, Supporting Information). The μ_m values reach about 2×10^3 μ_B for the original particles (NPs), and we note a decrease of about 20% for the **NC-3** and **NC-8** (exact values are given in Table S4). The reasonable variations of the particle magnetic moments suggest that the majority of the particle volume remains intact during the functionalization procedures. As we do not detect any extra paramagnetic phase in the samples (the ZFC and FC curves show strictly a single magnetic component), a rational explanation is that anchoring different ligands to the surface of the NPs causes changes to the spin structure in the surface layer, giving rise to the additional nonsaturating term in the magnetization isotherms and the about 20% decrease of the corresponding active "magnetic volume" (evidenced by the decrease of the μ_m). Alternatively, this observation can be attributed to the reduction of the mean physical size of the NPs during the coating procedure in comparison to the originally synthesized NPs. Such partial dissolution of the NPs and formation of Fe(III)-phosphonates due to strong interaction of phosphonic acid ligands and cosurfactants with Fe(III) surface ions was reported previously, and it could lead to high responsivity toward a magnetic field.[62] However, such dramatic overall reduction of the crystallite size was not observed in our samples (see the Supporting Information, Section 7). Also, the presence of the significant paramagnetic term in the magnetization isotherms of the modified NPs rather corroborates the ligand effect scenario.

Nevertheless, we would like to point out that the $T_B \sim K_{eff}V$, where V is the magnetically active volume of the particle proportional to the μ_m; thus a higher T_B for particles with a larger μ_m is expected. Moreover, the T_B typically decreases upon dilution of the magnetic NPs due to the increasing interparticle distance and thus the dipolar interparticle interactions. However, the increase of the T_B and the coercivity for the **NC-8** and **NC-3**, which have about 20% lower values of the μ_m, suggest that the ligand exchange causes significant spin disorder in the surface shell and enhancement of the K_{eff}. To our best knowledge, the observed "effect of coating" is among the most pronounced ever reported for nanoparticles modified with various organic ligands, including magnetic molecules.[52,63,64]

CONCLUSIONS

In this contribution, we report on a multistep synthesis of a chiral photosensitive trimeric ligand, which, in combination with a cosurfactant, efficiently stabilizes magnetic cobalt ferrite nanoparticles, giving rise to a stable non-aggregated nanomaterial. Upon doping into an achiral liquid crystalline host, the nanomaterial induces a chiral arrangement of mesophases of the liquid crystalline host, which has been documented by induced circular dichroism measurements. Moreover, the formed nanocomposite responds to illumination with UV light, which enables tuning of the supramolecular structures and, eventually, their transition to an isotropic liquid. The magnetic properties of the nanocomposite are rather weak due to the low concentration of the nanomaterial in the liquid crystalline host; however, we have observed an extremely strong effect of coating, which is unexpected among nanoparticles modified with organic ligands. In conclusion, the reported nanomaterial gives rise to chirality, photosensitivity, and magnetic properties in a liquid crystalline host at the same time. We propose that this type of magnetic NP-based dopants could be more efficient in modulating the properties of liquid crystals in comparison to a mixture of several dopants with the requested functionality. The resulting multifunctional liquid crystalline materials will enable dynamic tuning of their electromagnetic response *via* several stimuli, which is an important, yet unexplored, parameter to realize future applications of nanocomposites.

MATERIALS AND METHODS

Ligand Synthesis and Characterization. All reagents and dry DMF were purchased from commercial sources (Merck, TCI Chemicals, Acros Organics, Fluorochem Ltd., LachNer) and used without further purification. Tetrahydrofuran (THF) was distilled from sodium with the addition of benzophenone. For acylation reactions, dichloromethane (DCM) and toluene from a solvent purification system (PureSolv MD7) were used. Silica gel 60−100 μm (Merck) was used for column chromatography. For thin layer chromatography, TLC plates prepared in our laboratory using silica gel GF254 (Merck) or commercial TLC on a glass substrate from Merck was used. The structure of intermediates and final products was confirmed by IR spectroscopy (Thermo Scientific Nicolet iS10 FT-IR spectrometer on KBr discs indicated as KBr or using Bruker ALPHA FT-IR by the ATR technique indicated as film), NMR spectroscopy (Agilent 400-MR DDR2 spectrometer), mass spectrometry (LTQ-Orbitrap Velos from Thermo), and elemental analysis (PerkinElmer 2400 instrument). Melting points were measured using a Boetius apparatus from Leova.

Nanoparticles. Modification of NPs was performed using a Sonopuls HD 3200 ultrasound homogenizer. Modified NPs were investigated by elemental analysis (PE 2400 Series II CHNS/O analyzer), IR spectrometry (Nicolet 6700 spectrometer using the ATR technique, indicated as "film-NP"), TEM (JEOL JEM-1010 microscope with a SIS MegaView III digital camera), and TGA (Stanton-Redcroft TG 750, platinum container, in an inert nitrogen atmosphere with a heating rate of 5 °C·min^{-1}).

Nanocomposites. A solution of nanoparticles (0.15 mg) in $CHCl_3$ (2 mL) was sonicated at cooling using a US homogenizer for 15 min. An NP suspension was filtered through a syringe filter and added to the solution of an LC host (50 mg) in $CHCl_3$ (2 mL). The solvent was evaporated at 80 °C under an argon stream during 15 min of sonication in a US bath.

Induced Circular Dichroism Measurements. Solution CD and thin film CD spectropolarimetry were performed using an OLIS DCM 17 spectrophotometer suite using either a quartz cuvette (path length: 1 cm) for solution or flat precleaned quartz substrates for thin film experiments, respectively. Thin films for ICD spectropolarimetry were prepared between two quartz substrates separated by ∼10 μm Kapton tape spacers. Samples were rotated in 45° intervals from 0° to 315° (in the plane normal to the light beam) in order to differentiate CD absorption (reflection) from linear dichroism and birefringence.[21]

Photosensitivity. The *E*/*Z*-isomerization process was characterized by performing ^{1}H NMR measurements (Agilent 400-MR DDR2) of solutions (1.0×10^{-2} mol/L) during heating in NMR tubes or by UV−vis measurements (Varian Cary 50 UV−vis in quartz cuvettes). For UV−vis measurements, solutions of different concentrations of nanocomposites were prepared by dilution of a stock solution (1.5×10^{-3} mol/L) in chloroform (HPLC grade).

TEM Measurements. A drop of nanoparticle solution was deposited on a copper carbon-coated electron microscopic grid (400 mesh), and NPs were allowed to adhere for about 5 min. An excess of solution was removed by blotting the grid on filtration paper. After drying at room temperature, the grid was inserted into a JEOL JEM-1010 transmission electron microscope (JEOL, Japan), operated at 80 kV, and visualized by a Megaview III CCD camera and AnalySIS v 2.0 software (Olympus, Germany).

Magnetic Measurements. Bulk magnetic properties of the samples were measured using a properly calibrated MPMS XL-7 device (SQUID magnetometer, Quantum Design). The sample was placed in a gelatin capsule and fixed by polystyrene in a sample holder with a negligible background signal. The temperature dependence of

https://doi.org/10.1021/acsnano.1c10594
ACS Nano 2022, 16, 11833−11841

the ZFC and FC magnetization, $M(T)$, was recorded in the constant magnetic field of 10 mT with a step of 2 K after cooling the sample in the remnant field of the superconducting coil (below 0.5 mT). The magnetization isotherms were measured at 10 K and 300 K up to ±7 T. All magnetization data were normalized to the total mass of the measured sample to avoid an additional increase in the experimental error due to the normalization based on the cobalt ferrite content obtained by other analytical methods.

ASSOCIATED CONTENT

Supporting Information

The Supporting Information is available free of charge at https://pubs.acs.org/doi/10.1021/acsnano.1c10594.

Synthetic procedures leading to the ligands and characterization of their structure (^{1}H, ^{13}C, ^{31}P NMR, IR, elemental analysis, and MS spectra) as well as procedures for NP modification and their characterization (TEM images, IR spectra, and results of elemental and thermogravimetric analyses); description of UV−vis and ^{1}H NMR kinetic studies of ligand *E*/*Z*-isomerization and procedures of nanocomposite preparation and characterization (TEM and POM images, thin film CD spectra and magnetization data, and their analysis) (PDF)

AUTHOR INFORMATION

Corresponding Author

Michal Kohout − *Department of Organic Chemistry, University of Chemistry and Technology Prague, 16628 Prague 6, Czech Republic;* orcid.org/0000-0003-1447-4453; Email: michal.kohout@vscht.cz

Authors

Anna Poryvai − *Department of Organic Chemistry, University of Chemistry and Technology Prague, 16628 Prague 6, Czech Republic*

Michal Šmahel − *Department of Organic Chemistry, University of Chemistry and Technology Prague, 16628 Prague 6, Czech Republic*

Marie Švecová − *Department of Analytical Chemistry, University of Chemistry and Technology Prague, 16628 Prague 6, Czech Republic*

Ahlam Nemati − *Materials Science Graduate Program, Advanced Materials and Liquid Crystal Institute, Kent State University, Kent, Ohio 44242-0001, United States;* orcid.org/0000-0003-0282-2027

Sasan Shadpour − *Materials Science Graduate Program, Advanced Materials and Liquid Crystal Institute, Kent State University, Kent, Ohio 44242-0001, United States;* orcid.org/0000-0001-9736-7295

Pavel Ulbrich − *Department of Biochemistry and Microbiology, University of Chemistry and Technology Prague, 16628 Prague 6, Czech Republic*

Timothy Ogolla − *Materials Science Graduate Program, Advanced Materials and Liquid Crystal Institute, Kent State University, Kent, Ohio 44242-0001, United States*

Jiao Liu − *Materials Science Graduate Program, Advanced Materials and Liquid Crystal Institute, Kent State University, Kent, Ohio 44242-0001, United States*

Vladimíra Novotná − *Institute of Physics of the Czech Academy of Sciences, 182 21 Prague 8, Czech Republic*

Miroslav Veverka − *Department of Condensed Matter Physics, Charles University, 121 16 Prague 2, Czech Republic*

Jana Vejpravová − *Department of Condensed Matter Physics, Charles University, 121 16 Prague 2, Czech Republic;* orcid.org/0000-0002-6308-9992

Torsten Hegmann − *Materials Science Graduate Program, Advanced Materials and Liquid Crystal Institute, Kent State University, Kent, Ohio 44242-0001, United States; Brain Health Research Institute and Department of Chemistry and Biochemistry, Kent State University, Kent, Ohio 44242-0001, United States;* orcid.org/0000-0002-6664-6598

Complete contact information is available at: https://pubs.acs.org/10.1021/acsnano.1c10594

Author Contributions

The manuscript was written through contributions of all authors. All authors have given approval to the final version of the manuscript.

Notes

The authors declare no competing financial interest.

ACKNOWLEDGMENTS

This work was supported by Czech Science Foundation (project no. 19-03564S) and by the U.S. National Science Foundation (NSF, DMR-1904091) and the Ohio Third Frontier (OTF) program for Ohio Research Scholars: "Research Cluster on Surfaces in Advanced Materials" (T.H.). Magnetic and X-ray diffraction measurements were performed in MGML (mgml.eu), which is supported within the program of Czech Research Infrastructures (project no. LM2018096).

REFERENCES

(1) Schreivogel, A.; Dawin, U.; Baro, A.; Giesselmann, F.; Laschat, S. Chiral tetraphenylethenes as novel dopants for calamitic and discotic liquid crystals. *J. Phys. Org. Chem.* **2009**, *22* (5), 484−494.

(2) Superchi, S.; Donnoli, M. I.; Proni, G.; Spada, G. P.; Rosini, C. Induction of Cholesteric Mesophases by Simple Cyclic Derivatives of p,p'-Disubstituted 1,2-Diphenylethane-1,2-diols: Importance of Shape and Polarizability Effects. *J. Org. Chem.* **1999**, *64* (13), 4762−4767.

(3) Eelkema, R.; Feringa, B. L. Amplification of chirality in liquid crystals. *Org. Biomol. Chem.* **2006**, *4* (20), 3729−3745.

(4) di Matteo, A.; Todd, S. M.; Gottarelli, G.; Solladié, G.; Williams, V. E.; Lemieux, R. P.; Ferrarini, A.; Spada, G. P. Correlation between Molecular Structure and Helicity of Induced Chiral Nematics in Terms of Short-Range and Electrostatic-Induction Interactions. The Case of Chiral Biphenyls. *J. Am. Chem. Soc.* **2001**, *123* (32), 7842−7851.

(5) Gottarelli, G.; Proni, G.; Spada, G. P.; Fabbri, D.; Gladiali, S.; Rosini, C. Conformational and Configurational Analysis of 4,4'-Biphenanthryl Derivatives and Related Helicenes by Circular Dichroism Spectroscopy and Cholesteric Induction in Nematic Mesophases. *J. Org. Chem.* **1996**, *61* (6), 2013−2019.

(6) Yoshida, J.; Watanabe, G.; Kakizawa, K.; Kawabata, Y.; Yuge, H. Tris(β-diketonato) Ru(III) Complexes as Chiral Dopants for Nematic Liquid Crystals: the Effect of the Molecular Structure on the Helical Twisting Power. *Inorg. Chem.* **2013**, *52* (19), 11042−11050.

(7) Gutierrez-Cuevas, K. G.; Wang, L.; Xue, C.; Singh, G.; Kumar, S.; Urbas, A.; Li, Q. Near infrared light-driven liquid crystal phase transition enabled by hydrophobic mesogen grafted plasmonic gold nanorods. *Chem. Commun.* **2015**, *51* (48), 9845−9848.

(8) Bisoyi, H. K.; Li, Q. Light-Driven Liquid Crystalline Materials: From Photo-Induced Phase Transitions and Property Modulations to Applications. *Chem. Rev.* **2016**, *116* (24), 15089−15166.

(9) Martínez-Abadía, M.; Robles-Hernández, B.; de la Fuente, M. R.; Giménez, R.; Ros, M. B. Photoresponsive Cyanostilbene Bent-Core

Liquid Crystals as New Materials with Light-Driven Modulated Polarization. *Adv. Mater.* **2016**, *28* (31), 6586−6591.
(10) Malatesta, V.; Milosa, M.; Millini, R.; Lanzini, L.; Bortolus, P.; Monti, S. Oxidative degradation of organic photochromes. *Mol. Cryst. Liq. Cryst. Sci. Technol. Sect. A* **1994**, *246* (1), 303−310.
(11) Swansburg, S.; Choi, Y.-K.; Keum, S.-R.; Buncel, E.; Lemieux, R. P. Synthesis and characterization of liquid crystals containing a non-activated 1',3',3'-trimethylspiro\[2H-1-benzopyran-2,2-indoline] group. *Liq. Cryst.* **1998**, *24* (3), 341−346.
(12) Chen, S.; Li, W.; Zhu, W.-H. *Novel Ethene-Bridged Diarylethene Photochromic Systems: Self-Assembly, Photoswitcher, and Molecular Logic Gates*; Springer Japan: Tokyo, 2017.
(13) Bandara, H. M. D.; Burdette, S. C. Photoisomerization in different classes of azobenzene. *Chem. Soc. Rev.* **2012**, *41* (5), 1809−1825.
(14) Garcia-Amorós, J.; Szymczyk, A.; Velasco, D. Nematic-to-isotropic photo-induced phase transition in azobenzene-doped low-molar liquid crystals. *Phys. Chem. Chem. Phys.* **2009**, *11* (21), 4244−4250.
(15) Tamura, R.; Uchida, Y.; Suzuki, K., Editor: Li, Q. Magnetic Liquid Crystals. In *Liquid Crystals Beyond Displays: Chemistry, Physics and Applications*; Wiley & Sons: Hoboken, NJ, 2012; pp 83−110.
(16) Prakash, J.; Khan, S.; Chauhan, S.; Biradar, A. M. Metal oxide-nanoparticles and liquid crystal composites: A review of recent progress. *J. Mol. Liq.* **2020**, *297*, 112052.
(17) Romero-Hasler, P. N.; Kurihara, L. K.; Mair, L. O.; Weinberg, I. N.; Soto-Bustamante, E. A.; Martínez-Miranda, L. J. Nanocomposites of ferroelectric liquid crystals and FeCo nanoparticles: towards a magnetic response via the application of a small electric field. *Liq. Cryst.* **2020**, *47* (2), 169−178.
(18) Sebastian, N.; Lisjak, D.; Čopič, M.; Buchnev, O.; Mertelj, A. Comparison of dynamic behavior of ferroelectric and ferromagnetic nematic suspensions. *J. Mol. Liq.* **2018**, *267*, 377−383.
(19) Demortière, A.; Buathong, S.; Pichon, B. P.; Panissod, P.; Guillon, D.; Bégin-Colin, S.; Donnio, B. Nematic-like Organization of Magnetic Mesogen-Hybridized Nanoparticles. *Small* **2010**, *6* (12), 1341−1346.
(20) Stamatoiu, O. C.; Mirzaei, J.; Feng, X.; Hegmann, T. *Nanoparticles in Liquid Crystals and Liquid Crystalline Nanoparticles*; Wiley: Heidelberg, 2012; Vol. *318*.
(21) Mori, T.; Sharma, A.; Hegmann, T. Significant Enhancement of the Chiral Correlation Length in Nematic Liquid Crystals by Gold Nanoparticle Surfaces Featuring Axially Chiral Binaphthyl Ligands. *ACS Nano* **2016**, *10* (1), 1552−1564.
(22) Nemati, A.; Shadpour, S.; Querciagrossa, L.; Li, L.; Mori, T.; Gao, M.; Zannoni, C.; Hegmann, T. Chirality amplification by desymmetrization of chiral ligand-capped nanoparticles to nanorods quantified in soft condensed matter. *Nat. Commun.* **2018**, *9* (1), 3908.
(23) Nemati, A.; Shadpour, S.; Querciagrossa, L.; Mori, T.; Zannoni, C.; Hegmann, T. Highly Sensitive, Tunable Chirality Amplification through Space Visualized for Gold Nanorods Capped with Axially Chiral Binaphthyl Derivatives. *ACS Nano* **2019**, *13* (9), 10312−10326.
(24) Promiński, A.; Tomczyk, E.; Pawlak, M.; Jędrych, A.; Mieczkowski, J.; Lewandowski, W.; Wójcik, M. Size-Dependent Thermo- and Photoresponsive Plasmonic Properties of Liquid Crystalline Gold Nanoparticles. *Materials* **2020**, *13* (4), 875.
(25) Rahman, M. L.; Biswas, T. K.; Sarkar, S. M.; Yusoff, M. M.; Yuvaraj, A. R.; Kumar, S. Synthesis of new liquid crystals embedded gold nanoparticles for photoswitching properties. *J. Colloid Interface Sci.* **2016**, *478*, 384−393.
(26) Shukla, R. K.; Sharma, A.; Mori, T.; Hegmann, T.; Haase, W. Effect of two different size chiral ligand-capped gold nanoparticle dopants on the electro-optic and dielectric dynamics of a ferroelectric liquid crystal mixture. *Liq. Cryst.* **2016**, *43* (6), 695−703.
(27) Tomczyk, E.; Promiński, A.; Bagiński, M.; Górecka, E.; Wójcik, M. Gold Nanoparticles Thin Films with Thermo- and Photo-responsive Plasmonic Properties Realized with Liquid-Crystalline Ligands. *Small* **2019**, *15* (37), 1902807.
(28) Zep, A.; Wojcik, M. M.; Lewandowski, W.; Sitkowska, K.; Prominski, A.; Mieczkowski, J.; Pociecha, D.; Gorecka, E. Photo-tunable Liquid-Crystalline Phases Made of Nanoparticles. *Angew. Chem., Int. Ed.* **2014**, *53* (50), 13725−13728.
(29) Bhardwaj, A.; Sridurai, V.; Bhat, S. A.; Yelamaggad, C. V.; Nair, G. G. Photo-tunable epsilon-near-zero behavior in a self-assembled liquid crystal - nanoparticle hybrid material. *Nanoscale Adv.* **2021**, *3* (9), 2508−2515.
(30) Baldi, G.; Bonacchi, D.; Franchini, M. C.; Gentili, D.; Lorenzi, G.; Ricci, A.; Ravagli, C. Synthesis and Coating of Cobalt Ferrite Nanoparticles: A First Step toward the Obtainment of New Magnetic Nanocarriers. *Langmuir* **2007**, *23* (7), 4026−4028.
(31) Buathong, S.; Ung, D.; Daou, T. J.; Ulhaq-Bouillet, C.; Pourroy, G.; Guillon, D.; Ivanova, L.; Bernhardt, I.; Bégin-Colin, S.; Donnio, B. Thermal, Magnetic, and Luminescent Properties of Dendronized Ferrite Nanoparticles. *J. Phys. Chem. C* **2009**, *113* (28), 12201−12212.
(32) Daou, T. J.; Buathong, S.; Ung, D.; Donnio, B.; Pourroy, G.; Guillon, D.; Bégin, S. Investigation of the grafting rate of organic molecules on the surface of magnetite nanoparticles as a function of the coupling agent. *Sens. Actuators B: Chem.* **2007**, *126* (1), 159−162.
(33) Daou, T. J.; Grenèche, J. M.; Pourroy, G.; Buathong, S.; Derory, A.; Ulhaq-Bouillet, C.; Donnio, B.; Guillon, D.; Begin-Colin, S. Coupling Agent Effect on Magnetic Properties of Functionalized Magnetite-Based Nanoparticles. *Chem. Mater.* **2008**, *20* (18), 5869−5875.
(34) Sahoo, Y.; Pizem, H.; Fried, T.; Golodnitsky, D.; Burstein, L.; Sukenik, C. N.; Markovich, G. Alkyl Phosphonate/Phosphate Coating on Magnetite Nanoparticles: A Comparison with Fatty Acids. *Langmuir* **2001**, *17* (25), 7907−7911.
(35) Yee, C.; Kataby, G.; Ulman, A.; Prozorov, T.; White, H.; King, A.; Rafailovich, M.; Sokolov, J.; Gedanken, A. Self-Assembled Monolayers of Alkanesulfonic and -phosphonic Acids on Amorphous Iron Oxide Nanoparticles. *Langmuir* **1999**, *15* (21), 7111−7115.
(36) Poryvai, A.; Bubnov, A.; Pociecha, D.; Svoboda, J.; Kohout, M. The effect of the length of terminal n-alkyl carboxylate chain on self-assembling and photosensitive properties of chiral lactic acid derivatives. *J. Mol. Liqx.* **2019**, *275*, 829−838.
(37) Poryvai, A.; Vojtylová-Jurkovičová, T.; Šmahel, M.; Kolderová, N.; Tomášková, P.; Sýkora, D.; Kohout, M. Determination of Optical Purity of Lactic Acid-Based Chiral Liquid Crystals and Corresponding Building Blocks by Chiral High-Performance Liquid Chromatography and Supercritical Fluid Chromatography. *Molecules* **2019**, *24* (6), 1099.
(38) Prodanov, M. F.; Diakov, M. Y.; Vlasenko, G. S.; Vashchenko, V. V. Towards New Oligomesogenic Phosphonic Acids as Stabilizers of Nanoparticles Colloids in Nematic Liquid Crystals. *Synlett* **2015**, *26* (13), 1905−1910.
(39) Voigt, M.; Klaumünzer, M.; Ebel, A.; Werner, F.; Yang, G.; Marczak, R.; Spiecker, E.; Guldi, D. M.; Hirsch, A.; Peukert, W. Surface Functionalization of ZnO Nanorods with C60 Derivatives Carrying Phosphonic Acid Functionalities. *J. Phys. Chem. C* **2011**, *115* (13), 5561−5565.
(40) Prodanov, M. F.; Buluy, O. G.; Popova, E. V.; Gamzaeva, S. A.; Reznikov, Y. O.; Vashchenko, V. V. Magnetic actuation of a thermodynamically stable colloid of ferromagnetic nanoparticles in a liquid crystal. *Soft Matter* **2016**, *12* (31), 6601−6609.
(41) Battocchio, C.; Porcaro, F.; Mukherjee, S.; Magnano, E.; Nappini, S.; Fratoddi, I.; Quintiliani, M.; Russo, M. V.; Polzonetti, G. Gold Nanoparticles Stabilized with Aromatic Thiols: Interaction at the Molecule-Metal Interface and Ligand Arrangement in the Molecular Shell Investigated by SR-XPS and NEXAFS. *J. Phys. Chem. C* **2014**, *118* (15), 8159−8168.
(42) Pang, Z.; Zhang, J.; Cao, W.; Kong, X.; Peng, X. Partitioning surface ligands on nanocrystals for maximal solubility. *Nat. Commun.* **2019**, *10* (1), 2454.
(43) Arwin, H.; Schoeche, S.; Hilfiker, J.; Hartveit, M.; Järrendahl, K.; Juárez-Rivera, O. R.; Mendoza-Galván, A.; Magnusson, R. Optical

https://doi.org/10.1021/acsnano.1c10594
ACS Nano 2022, 16, 11833−11841

Chirality Determined from Mueller Matrices. *Appl. Sci.* **2021**, *11* (15), 6742.
(44) Laskarakis, A.; Logothetidis, S.; Pavlopoulou, E.; Gioti, M. Mueller matrix spectroscopic ellipsometry: formulation and application. *Thin Solid Films* **2004**, *455*−*456*, 43−49.
(45) Mendoza-Galván, A.; Muñoz-Pineda, E.; Ribeiro, S. J. L.; Santos, M. V.; Järrendahl, K.; Arwin, H. Mueller matrix spectroscopic ellipsometry study of chiral nanocrystalline cellulose films. *J. Opt.* **2018**, *20* (2), 024001.
(46) Albano, G.; Pescitelli, G.; Di Bari, L. Chiroptical Properties in Thin Films of π-Conjugated Systems. *Chem. Rev.* **2020**, *120* (18), 10145−10243.
(47) Li, L.; Salamończyk, M.; Shadpour, S.; Zhu, C.; Jákli, A.; Hegmann, T. An unusual type of polymorphism in a liquid crystal. *Nat. Commun.* **2018**, *9* (1), 714.
(48) Qi, H.; O'Neil, J.; Hegmann, T. Chirality transfer in nematic liquid crystals doped with (S)-naproxen-functionalized gold nanoclusters: an induced circular dichroism study. *J. Mater. Chem.* **2008**, *18* (4), 374−380.
(49) Shadpour, S.; Nemati, A.; Boyd, N. J.; Li, L.; Prévôt, M. E.; Wakerlin, S. L.; Vanegas, J. P.; Salamończyk, M.; Hegmann, E.; Zhu, C.; Wilson, M. R.; Jákli, A. I.; Hegmann, T. Heliconical-layered nanocylinders (HLNCs) - hierarchical self-assembly in a unique B4 phase liquid crystal morphology. *Mater. Horiz.* **2019**, *6* (5), 959−968.
(50) Sharma, A.; Mori, T.; Lee, H.-C.; Worden, M.; Bidwell, E.; Hegmann, T. Detecting, Visualizing, and Measuring Gold Nanoparticle Chirality Using Helical Pitch Measurements in Nematic Liquid Crystal Phases. *ACS Nano* **2014**, *8* (12), 11966−11976.
(51) van Rijssel, J.; Kuipers, B. W. M.; Erné, B. H. Non-regularized inversion method from light scattering applied to ferrofluid magnetization curves for magnetic size distribution analysis. *J. Magn. Magn. Mater.* **2014**, *353*, 110−115.
(52) Mikšátko, J.; Aurélio, D.; Kovaříček, P.; Michlová, M.; Veverka, M.; Fridrichová, M.; Matulková, I.; Žáček, M.; Kalbáč, M.; Vejpravová, J. Thermoreversible magnetic nanochains. *Nanoscale* **2019**, *11* (36), 16773−16780.
(53) Eloi, J. C.; Okuda, M.; Correia Carreira, S.; Schwarzacher, W.; Correia, M. J.; Figueiredo, W. Effective energy barrier distributions for random and aligned magnetic nanoparticles. *J. Phys.: Condens. Matter* **2014**, *26* (14), 146006.
(54) Pacakova, B.; Mantlikova, A.; Niznansky, D.; Kubickova, S.; Vejpravova, J. Understanding particle size and distance driven competition of interparticle interactions and effective single-particle anisotropy. *J. Phys.: Condens. Matter* **2016**, *28* (20), 206004.
(55) Peddis, D.; Cannas, C.; Musinu, A.; Ardu, A.; Orrù, F.; Fiorani, D.; Laureti, S.; Rinaldi, D.; Muscas, G.; Concas, G.; Piccaluga, G. Beyond the Effect of Particle Size: Influence of CoFe2O4 Nanoparticle Arrangements on Magnetic Properties. *Chem. Mater.* **2013**, *25* (10), 2005−2013.
(56) Brown, W. F. Thermal Fluctuations of a Single-Domain Particle. *J. Appl. Phys.* **1963**, *34* (4), 1319−1320.
(57) Coey, J. M. D. Noncollinear Spin Arrangement in Ultrafine Ferrimagnetic Crystallites. *Phys. Rev. Lett.* **1971**, *27* (17), 1140−1142.
(58) Mørup, S.; Brok, E.; Frandsen, C. Spin Structures in Magnetic Nanoparticles. *J. Nanomater.* **2013**, *2013*, 720629.
(59) Pacakova, B.; Kubickova, S.; Salas, G.; Mantlikova, A. R.; Marciello, M.; Morales, M. P.; Niznansky, D.; Vejpravova, J. The internal structure of magnetic nanoparticles determines the magnetic response. *Nanoscale* **2017**, *9* (16), 5129−5140.
(60) Hasz, K.; Ijiri, Y.; Krycka, K. L.; Borchers, J. A.; Booth, R. A.; Oberdick, S.; Majetich, S. A. Particle moment canting in $CoFe_2O_4$ nanoparticles. *Phys. Rev. B* **2014**, *90* (18), 180405.
(61) Krycka, K. L.; Borchers, J. A.; Booth, R. A.; Ijiri, Y.; Hasz, K.; Rhyne, J. J.; Majetich, S. A. Origin of Surface Canting within Fe_3O_4 Nanoparticles. *Phys. Rev. Lett.* **2014**, *113* (14), 147203.
(62) Lisjak, D.; Hribar Boštjančič, P.; Mertelj, A.; Mavrič, A.; Valant, M.; Kovač, J.; Hudelja, H.; Kocjan, A.; Makovec, D. Formation of Fe(III)-phosphonate Coatings on Barium Hexaferrite Nanoplatelets for Porous Nanomagnets. *ACS Omega* **2020**, *5* (23), 14086−14095.
(63) Lavorato, G.; Alzamora, M.; Contreras, C.; Burlandy, G.; Litterst, F. J.; Baggio-Saitovitch, E. Internal Structure and Magnetic Properties in Cobalt Ferrite Nanoparticles: Influence of the Synthesis Method. *Part. Part. Syst. Charact.* **2019**, *36* (4), 1900061.
(64) Vasilakaki, M.; Ntallis, N.; Yaacoub, N.; Muscas, G.; Peddis, D.; Trohidou, K. N. Optimising the magnetic performance of Co ferrite nanoparticles via organic ligand capping. *Nanoscale* **2018**, *10* (45), 21244−21253.

https://doi.org/10.1021/acsnano.1c10594
ACS Nano 2022, 16, 11833−11841